Microporous and Mesoporous Materials 175 (2013) 34–42

Contents lists available at SciVerse ScienceDirect

Microporous and Mesoporous Materials

journal homepage: www.elsevier.com/locate/micromeso

A combined computational and experimental study of high pressure and supercritical CO_2 adsorption on Basolite MOFs

Erhan Deniz [a], Ferdi Karadas [a], Hasmukh A. Patel [b], Santiago Aparicio [c,*], Cafer T. Yavuz [b,*], Mert Atilhan [a,*]

[a] Department of Chemical Engineering, Qatar University, Doha, Qatar
[b] Graduate School of EEWS, KAIST, Yuseong-gu, Daejeon, Republic of Korea
[c] Department of Chemistry, University of Burgos, Burgos, Spain

ARTICLE INFO

Article history:
Received 24 December 2012
Received in revised form 27 February 2013
Accepted 11 March 2013
Available online 25 March 2013

Keywords:
MOF
Basolite
CO_2 Adsorption
High-pressure FTIR
DFT

ABSTRACT

Metal organic frameworks (such as commercial Basolite®) display significant promise for CO_2 capture and storage. Here, in order to monitor CO_2 capture of Basolite®, we combined high pressure CO_2 adsorption with high-pressure FTIR and Monte Carlo simulations. We found that Basolite® C300 show an unprecedented rise in capture capacity above 25 bars, as predicted by the DFT calculations. Adsorption isotherms were measured up to 200 bar using a state-of-the-art magnetic suspension balance, and in-situ FTIR studies as a function of pressure allowed characterizing the preferential adsorption sites, and their occupancy with increasing pressure. Monte Carlo molecular simulations were used to infer nanoscopic information of the adsorption mechanism, showing the sorbent–CO_2 interactions from structural and energetic viewpoints.

1. Introduction

Increasing level of carbon dioxide (CO_2) in the atmosphere leading to a higher mean temperature is one of the biggest challenges of today's world [1]. If necessary actions are not taken, there will be consequences adversely affecting future generations. Our energy need continues to depend on burning fossil fuels like coal, oil and natural gas [2]. Although, atmospheric CO_2 predominantly comes from burning these natural sources, there is no economical alternative energy that can replace these. Since it is difficult to reduce CO_2 emissions by switching fuel sources, carbon capture and sequestration (CCS) technologies will be the main focus of ongoing research on CO_2 [3,4].

Currently, CO_2 capture processes rely on amine-based solvents like monoethanolamine [5,6], despite their disadvantages such as high regeneration cost and corrosive nature [7,8]. The high cost basically comes from the large energy requirement for regeneration of the captured CO_2 [9]. Roughly, 30% of the energy output of a power plant is spent for this purpose [10,11]. So, it becomes more important to develop solid CO_2 capture materials with lower regeneration costs.

CO_2 can be captured in three different known processes: pre-combustion, post-combustion and oxy-fuel combustion [12]. Each process has different conditions in terms of temperature and pressure and requires materials that have properties optimized for the respective process. Particularly, pre-combustion CO_2 capture needs materials that work under relatively high pressure and temperature.

A variety of porous materials have been studied for their CO_2 capture capacities such as activated carbons, zeolites, metal–organic frameworks (MOF) [13,14]. Zeolites [15] and activated carbons [16] are the most widely known solid materials for industrial CO_2 capture. Both type of adsorbents are generally used for relatively high-pressure capture processes. Moisture sensitivity of Zeolites requires high regeneration temperatures generally above 300 °C [17] and activated carbon lacks selectivity. MOFs, therefore, emerged as an alternative to these materials [18]. Their structural and chemical diversity makes them ideal materials in gas storage, separation and catalysis [19–22]. Recently, Long et al. reviewed MOFs for their CO_2 capture properties [23] showing that carbon dioxide capture with MOFs have been studied over a broad range of pressure and temperature conditions. Yildirim et al. investigated several MOFs to verify their efficiency of CO_2 capture in industrially relevant conditions like pressure swing adsorption or vacuum swing adsorption [24]. There have been several studies using MOFs for high-pressure gas sorption. Moellmer et al. studied HKUST-1 (Basolite® C300) for pressures as high as 50 MPa for hydrogen, carbon dioxide, nitrogen and methane storage purposes [25]. Long et al. used Mg–MOF-74 for high-pressure gas separations [26].

* Corresponding authors. Tel.: +974 44034142; fax: +974 44034131.
E-mail addresses: sapar@ubu.es (S. Aparicio), yavuz@kaist.ac.kr (C.T. Yavuz), mert.atilhan@qu.edu.qa (M. Atilhan).

1387-1811/$ - see front matter © 2013 Elsevier Inc. All rights reserved.
http://dx.doi.org/10.1016/j.micromeso.2013.03.015

Basolite® are commercial MOFs [27], which have recently been proposed as suitable compounds for CO_2 capture and gas treatment purposes [25,28,29]. In this work, we report a combined experimental and computational study about the CO_2 adsorption on three commercial Basolite® (C300, A100 and F300). Basic unit structures of these MOFs are given in Fig. S1 (ESI). Samples were characterized using several approaches and isothermal adsorption isotherms were measured up to 200 bars, which are among the highest studied pressure range for any MOF, using state-of-the-art magnetic suspension sorption apparatus. The mechanism of CO_2 adsorption was analyzed using IR spectroscopy as a function of pressure. Grand canonical Monte Carlo simulations allowed elucidation of the CO_2 adsorption mechanism from a nanoscopic viewpoint.

2. Experimental

2.1. Materials

Basolite® samples were obtained from Sigma–Aldrich, and no further purification was done. Basolite® C300 is structurally identical to HKUST-1 ($Cu_3(BTC)_2$, BTC = benzene-1,3,5-tricarboxylate) [25,30]. Basolite® A100 is isostructural to MIL-53-Al (aluminum terephthalate) [27]. The structure of Basolite® F300 is not fully clarified although it is claimed to be isostructural to MIL-100-Fe [31]. The pore and crystal structure of the studied MOFs is reported in Fig. 1. 99.99% pure CO_2 were used for adsorption tests provided by Buzwair Gas Company.

2.2. Characterization

The diffraction patterns of used samples were recorded using a Bruker D2 X-ray diffractometer at 30 kV and 300 mA. Measurements were performed for 2θ in the range of 5°–80° with a step size of 0.01° and scan speed of 2°/min. Scanning electron microscopy (SEM) pictures were acquired with a FEI Quanta 200 Environmental Scanning Electron Microscope (ESEM) with a resolution of 5 nm and a magnification ×200 K. In situ IR measurements as a function of applied pressure were carried out by using Bruker® Vertex 80 v FT-IR spectrometer coupled with Harrick® high pressure IR reflection cell.

2.3. Gas sorption measurements

A high-pressure magnetic suspension balance (MSB) sorption device manufactured by Rubotherm Präzisionsmesstechnik GmbH is used. Specifications of the instrument and the experimental procedure have been given elsewhere [32]. In this work, pressure up to 200 bars is used for maximum pressure and at the end of each isotherm, hysteresis check is conducted at each isotherm by collecting desorption data as the system is depressurized. CO_2 adsorption-desorption isotherms at 318, 328 and 338 K up to 200 bars were measured, Table S1 (ESI).

2.4. Computational details

The framework structures of the three studied Basolite® were built from unit cells crystal data obtained from the literature. Unit cell for C300 was from Chui et al. [33] (HKUST-1, Cambridge crystallographic databank CCDC 112954) and for A100 from Loiseau et al. [34] (MIL-53 (Al), CCDC 220475). Although the flexible character of MIL-53 (Al) has been widely discussed in the literature [35], we have used a fixed, rigid model for our Monte Carlo simulations of Basolite® A100, and thus breathing effect was not taken into consideration in our simulations. The structure of Basolite® F300 is still large unknown; [36] however, as Dhakshinamoorthy et al. [37] proposed, the structure of Basolite® F300 is expected to be close to that of MIL-100 (Fe) since both are iron 1,3,5-benzenetricarboxylates. Therefore we have used the unit cell data for MIL-100 (Fe) from Horcajada et al. [38] (CCDC 640536) as a model of Basolite® F300. Unit cells considered in the simulations are reported in Fig. 1. Supercells containing $2 \times 2 \times 2$ unit cells for C300 and F300, and $3 \times 4 \times 3$ unit cells for A100, which were all maintained rigid, were used along the simulations.

Lennard-Jones parameters for atoms in CO_2 and Basolite® sorbents were obtained from the Universal Force Field (UFF) [39]. Charges for framework atoms were obtained from the literature, whereas for CO_2 molecules $-0.35e$ on the O atoms and $+0.70e$ on the C atom were used [40]. All the used Lennard-Jones parameters are reported in Table S2 (ESI), whereas atomic charges are showed in Fig. S1 (ESI) together with the basic molecular structures for each Basolite®. Grand canonical Monte Carlo (GCMC) simulations were carried out at 318, 328 and 338 K, with 1×10^7 equilibration steps followed by 1×10^7 production steps to sample the desired thermodynamic properties, for each point calculated at a fixed CO_2 fugacity.

3. Results and discussion

High pressure adsorption studies using MSB equipment require knowledge of the density of the adsorbed gas on the pores to apply buoyancy corrections, and thus, to obtain absolute adsorbed amount, n (CO_2 buoyancy corrected), from the raw surface excess adsorbed amount (data without considering buoyancy corrections for adsorbed CO_2), n^σ. Several procedures were proposed in the literature to carry out these buoyancy corrections [41–44], and we applied the correction procedure proposed by Moellmer et al. [25] for all the data reported in this work, Table S1 (ESI). Absolute absorbed amounts are reported in Fig. 2 for the studied Basolite®, and compared with literature when available [25,45,46]. Values re-

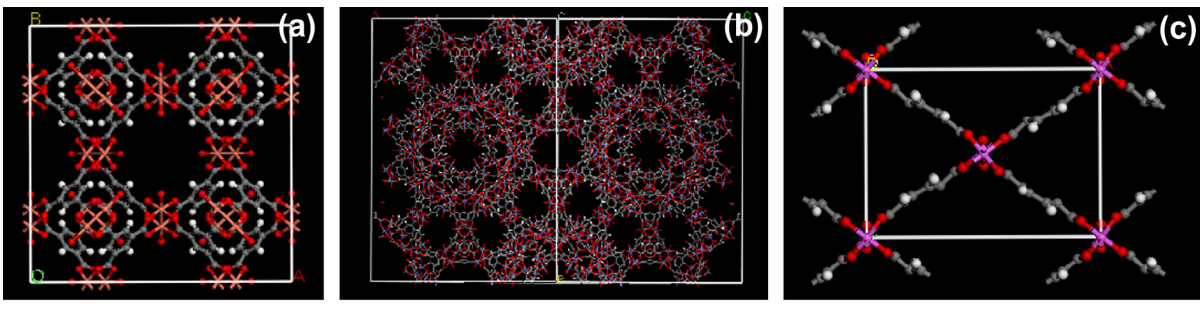

Fig. 1. Unit cells for Basolite®. The crystal system and space group for each unit cell is reported. In panel b, the structure is plotted in a way to allow the visibility of pores.

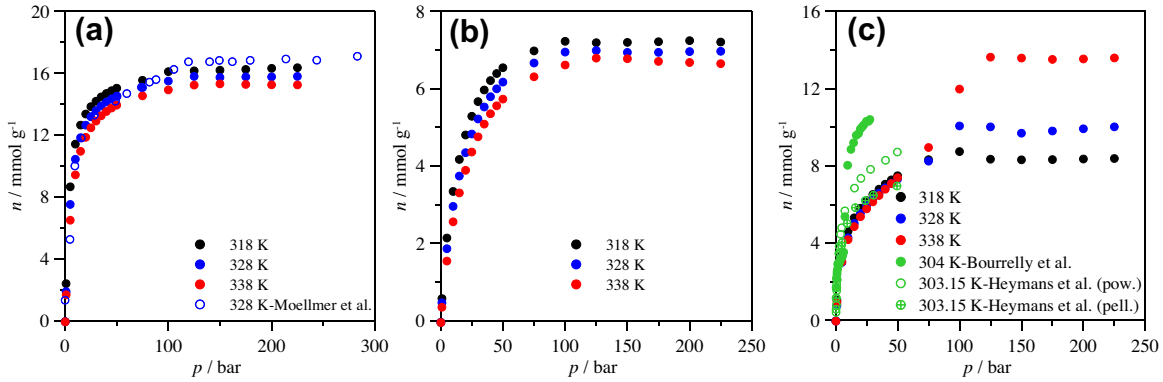

Fig. 2. Absolute (CO_2 buoyancy corrected) absorbed amount, n, on Basolite® (a) C300, (b) F300 and (c) A100. Literature data obtained from Moellmer et al. [25], Bourrelly et al. [45], and Heymans et al. [46]. Data from Heymans et al. use commercial Basolite A100 samples in powder and pellets forms.

ported in Fig. 2a for Basolite® C300 are in excellent agreement with those from Moellmer et al. [25], only some minor deviations were observed for pressures higher than 100 bar. We should remark that Moellmer et al. [25] used commercial powder Basolite® C300 (HKUST-1) samples for their measurements, as we did in this work. In the case of Basolite® F300, no data was found in the literature for this sorbent, and thus comparison was not possible. The behavior of Basolite® A100, both in its excess and absolute adsorption isotherm forms, show a highly anomalous behavior for pressures larger than 50 bar, Fig. 2c and Fig. S2 (ESI). The procedure used for data correction with absolute adsorbed amounts [25], leads to a temperature inversion for high-pressure regions. Likewise, the comparison of the data reported in this work for Basolite® A100, with those available in the literature show relevant conclusions, Fig. 2c. First, our data is in good agreement with those from Heymans et al. [46] for commercial Basolite® A100 in powder samples. Second, remarkable differences are obtained when using powder or pellet samples [46]. Third, data from Bourrelly et al. [45] are significantly different from those reported by Heymans et al. [46] and those in this work. The reason for this difference is the samples, which Bourrelly et al. [45] synthesized MIL-53 (Al) and we and Heymans et al. [46] used Basolite® A100 commercial supply. Although Basolite® A100 is also an aluminum terephthalate (MIL-53 (Al): $Al^{III}(OH)\cdot\{\}$), some difference appears between this commercial and non- commercial MIL-53 (Al) forms. Moreover, the behavior at low pressure between commercial and non-commercial forms of MIL-53 (Al) is different, the well-known breathing behavior of MIL-53 (Al), with the presence of a step around 6 bar [47,48], is not obtained for Basolite® A100, neither by Heymans et al. [46] nor in our data. Nevertheless, a possible breathing-related behavior seems to appear for pressures higher than 50 bars, Fig. 2c and Fig. S2 (ESI), which would justify the anomalous trends reported in Fig. 2c for that pressure range. We used crystal density of large pore (lp) MIL-53 (Al) structure for sorbent sample buoyancy correction (framework density of 0.94 g cm^{-3} from Assfour et al. [48]). Therefore, if some kind of structural change appears for the high-pressure region, crystal density would change, and so would the buoyancy corrections. Another possible reason could be due to the fact that physisorption of a gas adsorbed at low temperature may change into chemisorption at temperatures, due to the hydrogen bonding between the CO_2 molecule and MOF structure becomes more favorable then the weak van der Waals bonds on the adsorbent surface. However, this possibility is a weak possibility as no distinct change in power XRD results observed before and after the CO_2 measurements as well as there is no hysteresis on the adsorption–desorption data obtained from the sorption equipment.

The analysis of CO_2 adsorption results show capture ability in the order: Basolite® C300 > Basolite® A100–Basolite® F300. Although the molecular structure of units involved in Basolite® C300 and Basolite® F300, Fig. S1 (ESI), are identical (just replacing copper by iron atoms), the crystal structures, and thus, the pore sizes and distributions are very different between both compounds, Fig. 1, which, would justify the almost double CO_2 capture capacity of Basolite® C100 in comparison with Basolite® F300.

In order to assess the structural properties of the three studied Basolite®, and their possible relationship with the CO_2 adsorption ability, we calculated the accessible surface areas using the crystal models proposed for each compound in Fig. 1. The concept of surface area is controversial in the literature and several definitions have been proposed. Düren et al. [49] proposed the concept of accessible surface area, S_{acc}, to characterize crystalline solids for adsorption purposes, showing clearly better results to compare adsorbents than the commonly used Connolly surface area concept. Accessible surface area is calculated with a probe diameter corresponding to the adsorbate of interest. Therefore, we used a 3.30 Å probe diameter in this work, corresponding to the kinetic diameter of CO_2 molecules [50]. We applied the S_{acc} calculation procedure as described by He et al. [51] Free volumes were calculated both using a probe of CO_2 kinetic diameter, $V_{free,CO2}$, for measuring accessibility of CO_2 molecules to the available space, and using van der Waals radii of framework atoms, $V_{free,vdw}$, for measuring the total available space, Table 1. $V_{free,CO2}$ was obtained using a Monte Carlo integration procedure, Table 1, and compared with literature data when available [45,52–54]. The results reported in Table 1 show equivalent S_{acc} for C300 and F300, with slightly lower values for A100. The volume accessible to CO_2 molecules is also very similar for the three studied compounds when we compare the absolute values, but if we analyze the percentage of free volume compared with the total available volume, we obtain C300 > F300 > A100, in agreement with the CO_2 sorption ability for these compounds. The comparison between the calculated properties and those experimentally available shows differences in some cases, for example, BET surface area reported by Blanco et al. [53] for the three studied Basolite® are almost the half as those calculated in this work. Other available results (Table 1), however, are in close agreement with our calculations. Haque et al. [55] reported huge changes in BET surface area for MIL-53 (Al) (Basolite®A100 model) with purification conditions, with values ranging from 143 to 1425 m^2 g^{-1}. Therefore, the preparations of the samples could justify the differences between the literature sources. Nevertheless, the values reported in Table 1 may be considered as reasonable, concluding similar accessible sorption surface for C300 and F300 crystal models, and slightly lower

Table 1
Calculated accessible surface area, S_{acc}, CO_2 accessible free volume, $V_{free,CO2}$, and free volume (calculated from the framework van der Waals radii), $V_{free,vdw}$ for the studied Basolite®. The values in parentheses show the percentage of corresponding free volume compared with the total volume available (free+occupied).

Compound	S_{acc} m^2 g^{-1}	ρ_{bulk} g cm^{-3}	$\rho_{crystal}$ g cm^{-3}	Pore size nm	Pore volume cm^3 g^{-1}	$V_{free,CO2}$ cm^3 g^{-1}	$V_{free,vdw}$ cm^3 g^{-1}
C300	1706.42[a] 1798[b] 1277[c]	0.35[f]	0.958	0.61[c]	6.1[c]	0.122 (17.4%)	0.721 (68.4%)
F300	1716.46[a] 840[d] 854[c]	0.30[f]	0.98	0.60[c]	6.0[c]	0.179 (14.0%)	0.630 (42.86%)
A100	1524.8[a] 1500[e] 662[c]	0.40[f]	1.61	0.53[c]	5.5[c]	0.130 (13.0%)	0.581 (57.8%)

[a] BET measurements for this work.
[b] BET surface area from Sava et al. [52].
[c] BET surface area from Blanco et al. [53].
[d] BET surface area from Dhakshinamoorthy et al. [54].
[e] Langmuir surface area from Bourrelly et al. [45].
[f] Tapping density values.

(approximately around 11%) for A100 crystal model. The differences between each of the experimental CO_2 adsorption are not only due to the spatial properties of the sorbents. In the light of these, we report in Fig. 3 the available accessible volume in the studied Basolite®. The distribution of available spaces (pores distribution) is very different between C300 and F300. In the case of C300, the available space is symmetrical around the main channels, blue areas in Fig. 3a, and thus, we may expect that most of the CO_2 molecules concentrate in these channels because adsorption around Cu atoms seems to be spatially hindered. In the case of F300 (MIL-53 (Fe) as model), the large mesoporous cages accessible through microporous windows are clearly visible. For Basolite® A100, in its large pore structure, the large channels are visible, although their diameter is lower than for C300, which could justify lower adsorption ability for CO_2 molecules.

Isosteric heat of adsorption, ΔH_S, was obtained from experimental (absolute) absorbed amounts using the Clausius–Clapeyron equation and a procedure described previously [32]. The Padé equation was used to fit the experimental adsorption data to obtain isosteric data for using in the Clausius–Clapeyron equation, Table S3 (ESI) [25]. ΔH_S data reported in Fig. 4 follow the order: C300 > F300 > A100. Values obtained for C300 in this work are lower than those reported by Moellmer et al. [25] On the other hand, Keskin et al. [56] reported that literature available data for HKUST-1 (Basolite C300) range from 35 to 12 kJ mol^{-1}, and justified these differences considering the different types of making the samples and sorbent activation processes.

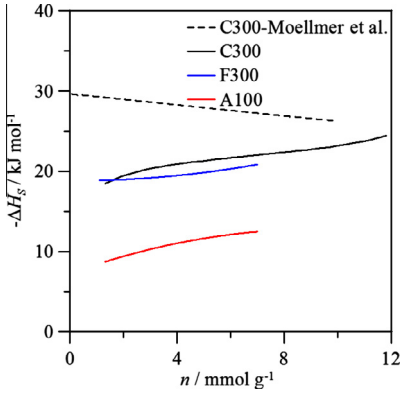

Fig. 4. Isosteric heat of adsorption, ΔH_S, for CO_2 on Basolite® calculated using the absolute amount adsorbed and the Clausius–Clapeyron equation coupled with Padé fittings of experimental data. We also report data from Moellmer et al. [25].

Heymans et al. [46] reported significant differences between the CO_2 adsorption on Basolite® A100 in powder and pellet samples. Therefore, we carried out a Basolite® particle characterization before and after CO_2 adsorption from SEM nanographs, Fig. 5 and Figs. S3–S5. Khvostikova et al. [57] also reported SEM results for Basolite® C300 showing no agglomeration but homogeneous distribution in the micrometer ranges. Lamia et al. [30] reported polycrystalline agglomerates in the 5–10 μm range, interspersed with octahedral-shaped crystals. Basu et al. [58] reported particle size

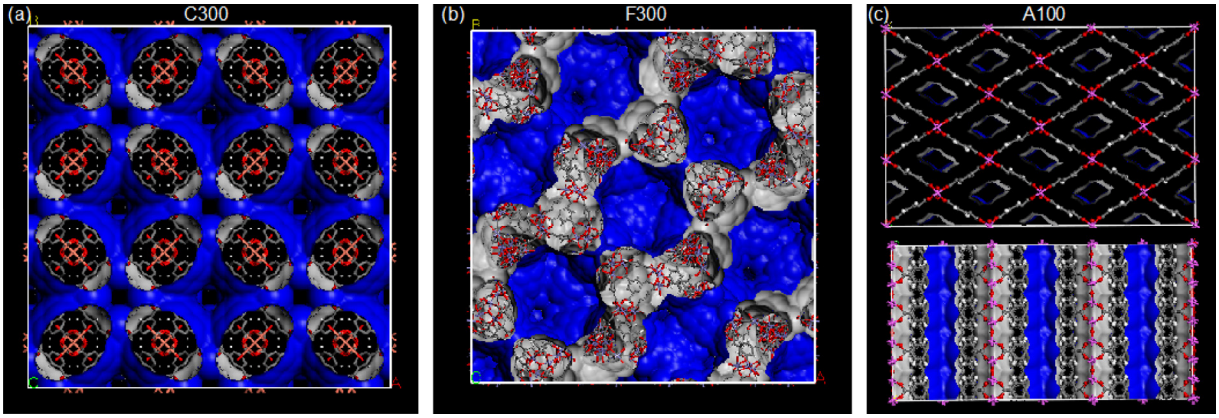

Fig. 3. Free volume in the studied Basolite®. The structure of Basolite® A100 is viewed along two different planes to allow full visualization.

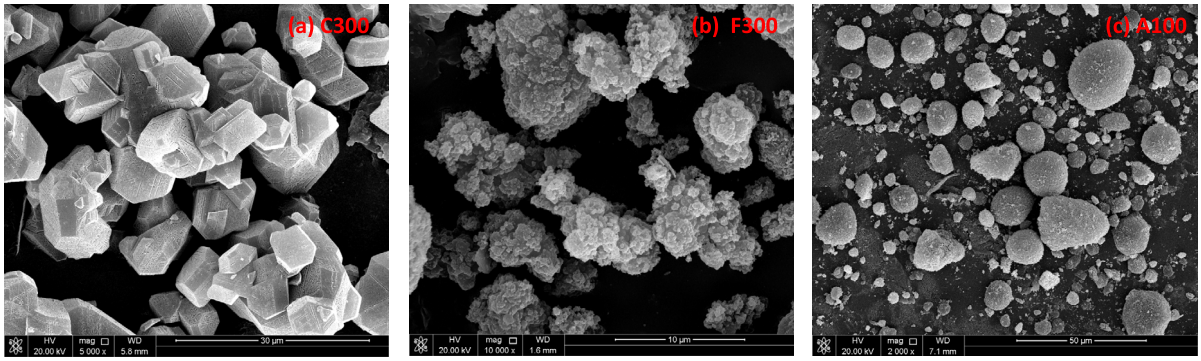

Fig. 5. SEM nanographs for the studied Basolite®.

in the 10–15 and <200 μm ranges for Basolite® C300 and A100, respectively. To the best of our knowledge no data on particle sizes for Basolite® F300 is available in the literature. The data provided by the commercial supplier are 15.96 μm and 31.55 μm particle size for Basolite® C300 and A100, respectively. The SEM results reported in this work for Basolite® C300, Fig. 5a, show particle size distribution <30 μm, where the closest nanograph in the submicrometer range, Fig. S4 (ESI) show that agglomeration of nanospheres. In the case of Basolite® F300, Fig. 5b, particle size distribution in the 5–10 μm range is obtained, with poorly defined shapes in contrast with those for Basolite® C300. The submicrometer structure for Basolite® F300, Fig. S5 (ESI) is also clearly different to that for Basolite® C300, showing globular aggregates. Basolite® A100, Fig. 5c, shows a large particle size distribution, 5–30 μm range, with globular particles aggregation in the submicrometer range, Fig. S5 (ESI). Results reported in Figs. S3–S5 (ESI) show no remarkable changes in particle distribution upon CO_2 adsorption, which show that these adsorbents could be used in sorption-desorption cycles without changing their structural properties.

The analysis of the main features of IR spectra of adsorbed CO_2 in the studied compounds is generally used to extract the adsorption mechanism and its possible changes with increasing pressure. In a recent study, Kauffman et al. [59] showed the strengths of in situ IR studies to get valuable information on the CO_2 pore filling mechanism and structural changes upon adsorption in MOFs, which were in agreement with previous studies [60,61]. In the case of CO_2 molecules adsorbed in MOFs, the changes of two main CO_2 frequencies upon adsorption lead to valuable information: (i) ν_3 antisymmetric stretching (appearing at 2349 cm^{-1} in the gas phase) and (ii) ν_2 bending mode (667 cm^{-1} gas phase value) [58]. Bordiga et al. [60] showed ν_3 redshifting on HKUST-1, and concluded with the presence of two different copper interaction sites. To the best of our knowledge, systematic in-situ studies of CO_2 adsorption on Basolite® F300 and A100 are not available in the literature. The IR spectra was collected in the 400–4000 cm^{-1} as a function of applied pressure at 318 K. Useful features were obtained in the 2200–2500 cm^{-1} range, corresponding to the CO_2 ν_3 antisymmetric stretching mode, and in the 3500–3800 cm^{-1}, corresponding to the CO_2 combination mode ν_1 (symmetric stretching) + ν_3, Fig. S6 (ESI) [60]. No information could be extracted from the region corresponding to ν_2 (CO_2 bending) because it was not possible to resolve it. No remarkable features are obtained in the remaining spectral regions. Results reported in Fig. S6 (ESI) show increasing intensities in the $\nu_1 + \nu_3$ and ν_3 spectral regions with increasing pressure, corresponding to increasing CO_2 adsorbed amounts. The ν_3 region is characterized by the split of this mode into two peaks at 2340 and 2358 cm^{-1}, Fig. 6b, with almost negligible difference for the three studied Basolite®, with the intensities in agreement with the CO_2 adsorption abilities of the studied compounds. Bordiga et al. [60] reported these bands at 2333 and 2342 cm^{-1} on non-commercial HKUST-1, which are slightly lower than the values obtained in this work for commercial Basolite® C300. The lower frequency band is redshifted whereas the higher frequency band is blueshifted with respect to the CO_2 ν_3 antisymmetric stretching band in gas phase. Although the ν_3 band split is obtained for each of the three studied Basolite® (Fig. 5), the relationship between the intensities of both splitted bands is very different. For Basolite® C300, for low pressures only the 2333 cm^{-1} band is obtained and only for large pressures a shoulder corresponding to the 2342 cm^{-1} is obtained. Bordiga et al. [60] attributed the low frequency ν_3 band to interactions with internal copper sites and the high frequency to external sites, therefore, in the case of Basolite® C300 the second type of sites are only occupied with increasing pressures. In the case of Basolite® F300 and Basolite® A100, the intensity ratio of both peaks is more similar, showing analogous occupation of both interacting sites with increasing pressure.

The $\nu_1 + \nu_3$ spectral region is shown in Fig. 6a. The intensities of the peaks are lower than those for the ν_3 region for pressures lower than 1000 mbar, only for higher pressures both spectral regions reach similar levels. This spectral region shows features around the 3600 and 3700 cm^{-1} regions with two peaks in each region appearing at almost the same frequencies for the three studied compounds. The high frequency features (3703 and 3728 cm^{-1}) dominate over the low frequency ones (3599 and 3628 cm^{-1}), especially for the high-pressure adsorption, Fig. S6 (ESI).

In short, FTIR results show the existence of two different adsorption sites in the three studied Basolite®, and to show the evolution of the occupancy of each site in a quantitative way, we have plotted (Fig. 7) the evolution of intensities with increasing pressure, at the fixed wavenumbers reported in Fig. 6. The reported results show that intensities in the ν_3 spectral region are 30% larger for Basolite® C300 than for F300 and A100. The changes of ν_3 intensities reach saturation with increasing pressure for the three studied compounds, whereas those for the $\nu_1 + \nu_3$ peaks increase in linear way, leading to more intense peaks than those for the ν_3 mode in the higher pressure regions.

Monte Carlo simulations reported in this work would help to understand the CO_2 adsorption mechanism from a nanoscopic viewpoint. The validation of the proposed computational approach was done through the comparison between calculated and experimental adsorption isotherms in the studied pressure – temperature ranges, Fig. S7 (ESI). An excellent agreement is found between predicted and experimental isotherms, especially for C300 and F300 sorbents. It should be noted that the crystal model used to mimic F300 structure (based on MIL-100 (Fe)) leads to accurate predictions, and thus confirming the possible structural

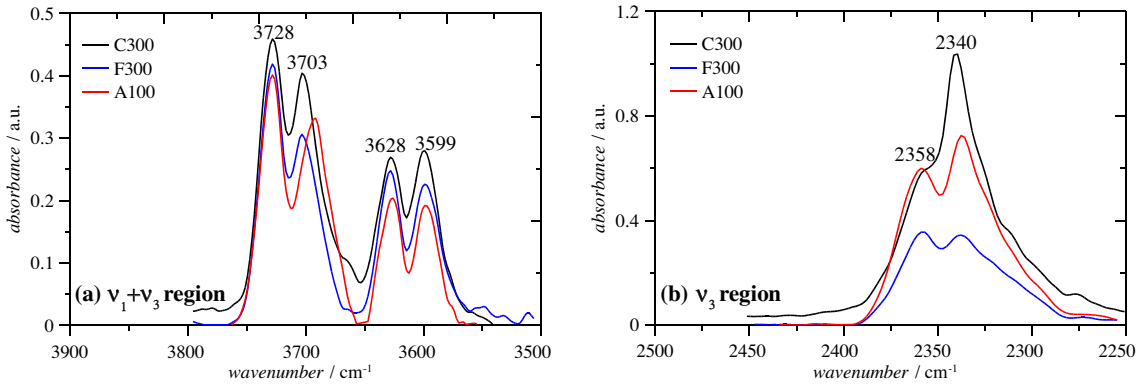

Fig. 6. IR spectra of CO_2 adsorbed in the studied Basolite®, in the (a) $\nu_1 + \nu_3$ combination band and (b) ($\nu_1 + \nu_3$ combination band spectral regions. Results reported at 318 K and (a) 1000 mbar and (b) 200 mbar.

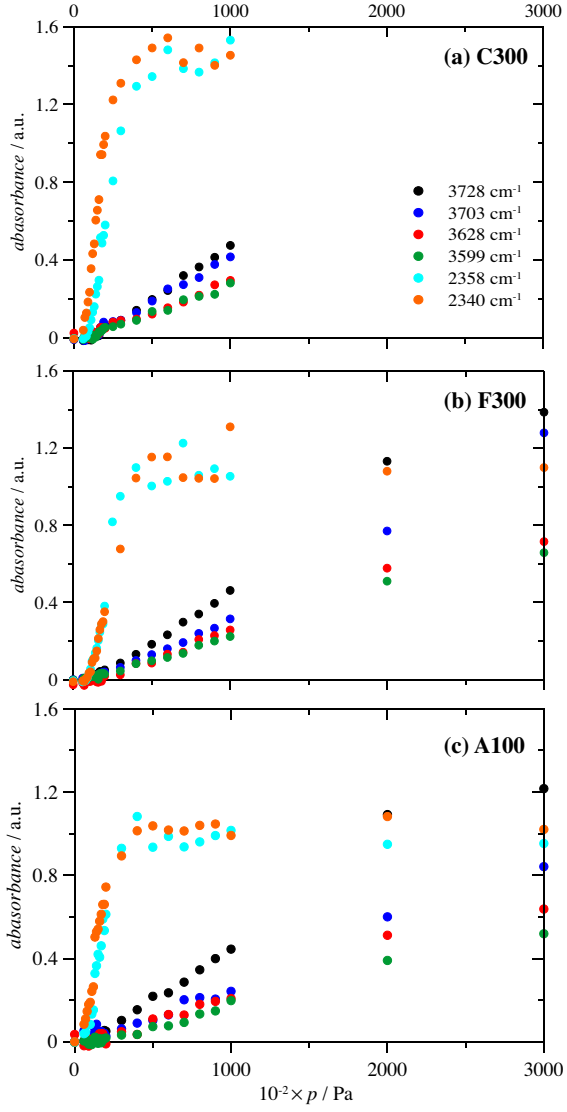

Fig. 7. Peak intensity evolution as a function of pressure for CO_2 adsorbed on Basolite® at 318 K, for the peak values reported in Fig. 6.

proximity between MIL-53 (Fe) and Basolite® F300. The poorest predictions exist for Basolite® A100, especially for pressures larger than 50 bar, which in our opinion rises from the rigid structural crystal model used in the simulations. This is the reason why we are not taking into account the structural flexibility for pressures lower than 6 bar (the well-known breathing effect with narrow pore to large pore transition) [45,47] and the complex experimental behavior obtained for pressures larger than 50 bar. Nevertheless, the simulations predict correctly the CO_2 adsorption ability ordering of the studied compounds, with the largest CO_2 adsorption for C300, and a good quantitative agreement is also obtained.

The analysis of CO_2 molecules in Basolite® structures may be done using the isodensity plots reported in Fig. 8 as a function of pressure. Results for Basolite® C300, Fig. 8a and b, show that for low pressure, CO_2 molecules concentrate in the larges pores following an axial distribution as the blue dashed line in Fig. 8a. With increasing pressure the large pores are completely filled with CO_2 molecules, blue arrow in Fig. 8b, and at the same time octahedral pockets (pores close to Cu–Cu bonds) are also filled with CO_2 molecules, green arrow in Fig. 8b. The tetrahedral pores and the vicinity of the benzene rings remain almost free of CO_2 molecules, Fig. 8b. This situation is reverse to the adsorption of other molecules in HKUST-1 (Basolite® C300). Lamia et al. [30] reported that for the adsorption of hydrocarbons, the small octahedral pockets are occupied first and once they are filled, large cages are filled. For Basolite® F300 (MIL-100 (Fe) model) the CO_2 adsorption (Fig. 8c and d) does not show remarkable differences between the way in which different adsorption sizes are occupied, but rather a homogeneous distribution is obtained, increasing with elevated pressures. A comparison of results reported in Fig. 8b and d for Basolite® C300 and F300 shows clearly the higher concentration of CO_2 molecules in the available pores of C300 in comparison with those for F300. The rigid model for Basolite A100 (Fig. 8e and f), with large pores, led to CO_2 molecules occupying the available pores in even–odd distributions along the channels, in agreement with the free volume reported in Fig. 3c. CO_2 molecules follow a distribution reported in Fig. 8f, yellow dashed lines, in which molecules arrange in a parallel-antiparallel way for neighboring pores, increasing its concentration with increasing pressure. This different distribution for even–odd channels were previously reported for methane molecules in MIL-53 (Al) and was explained considering antiparallel alignments of the OH groups in the inorganic octahedra [62]. In this spatial arrangement, the interaction of CO_2 molecules with OH groups is allowed, as previously reported by Ramsahye et al. [63] To analyze the properties of adsorbed CO_2 molecules, radial distribution functions (RDFs) for CO_2–CO_2 pairs, and the corresponding running integrals, are reported in Fig. 9. Reported RDFs show strong first peaks at 3.9, 4.5 and 4.9 Å for Basolite® C300, F300 and A100. The intensity of these first RDFs peaks, and thus, the values of the corresponding running

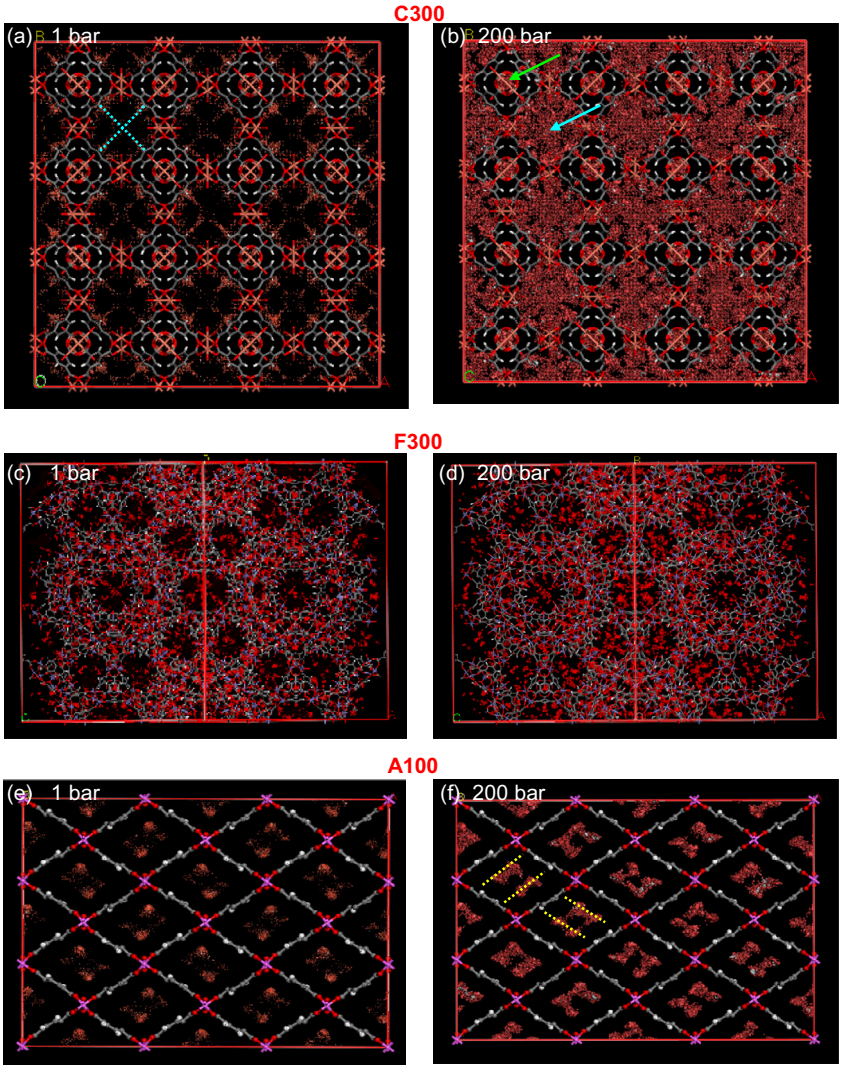

Fig. 8. Calculated isodensity surfaces (red surfaces) for CO_2 molecules in the studied Basolite® at 318 K and 1 and 200 bar. Dashed lines and arrows indicate notable adsorption features.

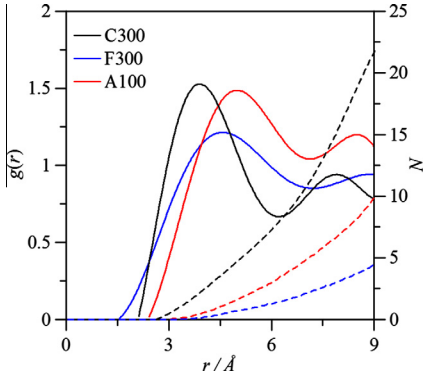

Fig. 9. Radial distribution functions, *g(r)*, between the center-of-mass of CO_2 adsorbed molecules in the studied Basolite® at 318 K and 200 bar. Running integrals, *N*, are also reported for each *g(r)*.

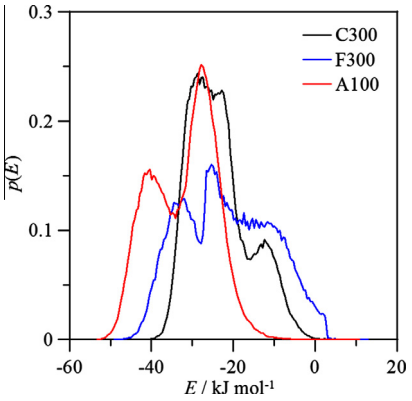

Fig. 10. Probability distribution functions, *P(E)*, for CO_2–Basolite® interaction energies at 328 K – 20 bar obtained from Monte Carlo simulations.

integrals follows the ordering of adsorption abilities reported in Fig. 2. Likewise, these first RDFs peaks show that CO_2 distribution within the sorbents pores reported in Fig. 8 correspond to high density CO_2 layers obtained at the studied high pressures. Moreover, results reported in Fig. 9 show that the proposed parameterization is able to describe the CO_2 adsorption even in the very high pressure regions.

In order to assess the affinity between the CO_2 molecules and the corresponding sorbents, we calculated the distribution func-

tions of CO_2–sorbent interaction energies from Monte Carlo simulations. We report a comparison between the distribution of interaction energies for the three studied Basolite® in Fig. 10. In the case of Basolite® C300, two peaks are identified to be −28 and −12 kJ mol^{-1}, the adsorption in large cages and octahedral pockets, respectively. For Basolite® F300, a wide band is obtained, and two peaks at −25 and −32 kJ mol^{-1}, being in agreement with the distribution reported in Fig. 8, where no preferential adsorption sites were found. In the case of Basolite® A100, two peaks at −28 and −40 kJ mol^{-1} are obtained. Considering that the pores are all alike, these two peaks can only be assigned to adsorption in even and odd channel with different interaction energies rising from the position of hydroxyl groups in the sorption framework. The effect of pressure on the distribution of interaction energies is reported in Fig. S8 (ESI). Wider bands are obtained in all the cases, with decreasing peaks for the highest energies and increasing ones for the lowest energies, corresponding to increasing occupancies of less favorable adsorption sites. The values reported in Fig. 10 show larger CO_2–sorbent interaction energies for A100 than for C300 or F300 compounds, which is in contrast with CO2 adsorption ordering reported in Fig. 2 and with the isosteric heats of adsorption reported in Fig. 4 (lower for A100 than for C300 and F300). Values reported in Fig. 10 show CO_2–sorbent interaction energies, whereas isosteric heat of adsorption rises reported in Fig. 4 rises not only from CO_2–sorbent interactions but also from CO_2–CO_2 interaction energies, which are specially important when high pressure region is reached. The higher density of CO_2 molecules in C300 pores in comparison with A100 and F300 reported in Figs. 8 and 9, would justify the largest heats of adsorption for this compound in spite of the lower CO_2–sorbent interaction energies.

We also calculated adsorption enthalpies from Monte Carlo simulations (Fig. S9), with the largest values (around 17 kJ mol^{-1}) obtained for MIL-53 (Al) (Basolite® A100 model). This value is in good agreement with previous simulations and microcalorimetric measurements for large pore structure of MIL-53 (Al) reported by Ramsahye et al. [63], and it remains almost constant up to 200 bar. For Basolite® C300 and F300, heat of adsorption is around −25.6 and −24.0 kJ mol^{-1}, respectively. In the case of F300, heat of adsorption decreases from −30 kJ mol^{-1} to −24.0 kJ mol^{-1} in the 0–20 bar range, and then it remains almost constant up to 200 bars. Farruseng et al. [64] reported experimental and simulated heat of adsorption for CO_2 molecules in HKUST-1 (Basolite® C300), their simulated values (−21.8 kJ mol^{-1}) are larger than the experimental values (from −12.1 to −14.6 kJ mol^{-1}, depending on the measurement technique) reported by the same authors. Farruseng et al. [64] justified the differences between experimental and simulated results by considering that small pores (which would increase adsorption enthalpy because of larger sorbent–CO_2 interactions) are not experimentally accessible. Our results reported in Fig. 8 confirm that small pores are only fully occupied when pressure increases. In our opinion, the larger CO_2 sorption ability of Basolite® C300 in comparison with Basolite® F300 and Basolite® A100, rises from the ability to occupy largest pores together with small octahedral pockets. This leads to an almost condensation of CO_2 molecules within these adsorption sites, (Fig. 8b), as it is also inferred from RDFs reported in Fig. 9. On the contrary, available pores in F300/A100 are only partially occupied, leading to lower sorption ability for these compounds. The sizable free volume available should then be in control for the adsorption at high loadings [65].

4. Conclusions

The CO_2 adsorption on commercial Basolite® was studied using a wide collection of experimental and computational approaches and extended to the high-pressure region for the first time. The three studied compounds (C300, F300 and A100) show remarkable different structural properties and adsorptive ability, being the CO_2 capturing ability in the order of C300 > F300–A100. The high-pressure adsorption studies show saturation behavior for pressures larger than 50 bars, a previously unknown observation. Likewise, an anomalous behavior for Basolite A100® is obtained in the high-pressure range, which is attributed to structural changes. IR studies have showed the existence of two different adsorption sites for the studied compounds, which is confirmed by the molecular simulation results. The changes in the occupancy of adsorption sites determine the sorption ability for the studied compounds. Moreover, no structural changes are observed after CO_2 adsorption, making these compounds, especially Basolite® C300 to have very suitable properties for CO_2 capture.

Acknowledgements

This paper was made possible by the support of an NPRP grant (No.: 08-670-1-124) from the Qatar National Research Fund. The statements made herein are solely the responsibility of the authors.

Appendix A. Supplementary data

Supplementary data associated with this article can be found, in the online version, at http://dx.doi.org/10.1016/j.micromeso.2013.03.015.

References

[1] D.Q.S. Solomon, M. Manning, Z. Chen, M. Marquis, K.B. Averyt, M. Tignor, H.L. Miller, Contribution of Working Group I to the Fourth Assessment Report of the Intergovernmental Panel on Climate Change, Cambridge University Press, Cambridge, United Kingdom, 2007.
[2] Annual Energy Outlook 2011, U.S. Energy Information Administration, Washington, DC, 2011.
[3] C.W. Jones, Annu. Rev. Chem. Biomol. 2 (2011) 31–52.
[4] I.D.S.G.S.M. Benson, D. Cahen, Fundamentals of Materials for Energy and Environmental Sustainability, Cambridge University Press, 2012.
[5] R.N.A. Kohl, Gas Purification, Gulf Professional Publishing, Houston, TX, 1997.
[6] G.T. Rochelle, Science 325 (2009) 1652–1654.
[7] S. Ma'mun, H.F. Svendsen, K.A. Hoff, O. Juliussen, Energy Convers. Manage. 48 (2007) 251–258.
[8] M.S. Dupart, T.R. Bacon, D.J. Edwards, Hydrocarbon Process. 72 (1993) 89.
[9] F.Y. Jou, A.E. Mather, Int. J. Thermophys. 28 (2007) 490–495.
[10] J. Davison, K. Thambimuthu, Proc. Inst. Mech. Eng. A–J Pow 223 (2009) 201–212.
[11] J.P. Ciferno, T.E. Fout, A.P. Jones, J.T. Murphy, Chem. Eng. Prog. 105 (2009) 33–41.
[12] J.D. Figueroa, T. Fout, S. Plasynski, H. McIlvried, R.D. Srivastava, Int. J. Greenhouse Gas Control 2 (2008) 9–20.
[13] S. Choi, J.H. Drese, C.W. Jones, ChemSusChem 2 (2009) 796–854.
[14] D.M. D'Alessandro, B. Smit, J.R. Long, Angew. Chem. Int. Ed. 49 (2010) 6058–6082.
[15] R. Krishna, J.M. van Baten, Sep. Purif. Technol. 87 (2012) 120–126.
[16] M. Sevilla, A.B. Fuertes, Energy Environ. Sci. 4 (2011) 1765–1771.
[17] P.J.E. Harlick, A. Sayari, Ind. Eng. Chem. Res. 45 (2006) 3248–3255.
[18] N.L. Rosi, J. Kim, M. Eddaoudi, B.L. Chen, M. O'Keeffe, O.M. Yaghi, J. Am. Chem. Soc. 127 (2005) 1504–1518.
[19] G. Ferey, Chem. Soc. Rev. 37 (2008) 191–214.
[20] S. Kitagawa, R. Matsuda, Coord. Chem. Rev. 251 (2007) 2490–2509.
[21] D. Bradshaw, J.B. Claridge, E.J. Cussen, T.J. Prior, M.J. Rosseinsky, Acc. Chem. Res. 38 (2005) 273–282.
[22] M.J. Rosseinsky, Microporous Mesoporous Mater. 73 (2004) 15–30.
[23] K. Sumida, D.L. Rogow, J.A. Mason, T.M. McDonald, E.D. Bloch, Z.R. Herm, T.H. Bae, J.R. Long, Chem. Rev. 112 (2012) 724–781.
[24] J.M. Simmons, H. Wu, W. Zhou, T. Yildirim, Energy Environ. Sci. 4 (2011) 2177–2185.
[25] J. Moellmer, A. Moeller, F. Dreisbach, R. Glaeser, R. Staudt, Microporous Mesoporous Mater. 138 (2011) 140–148.
[26] Z.R. Herm, R. Krishna, J.R. Long, Microporous Mesoporous Mater. 157 (2012) 94–100.
[27] U. Mueller, M. Schubert, F. Teich, H. Puetter, K. Schierle-Arndt, J. Pastre, J. Mater. Chem. 16 (2006) 626–636.

[28] J. Liu, P.K. Thallapally, B.P. McGrail, D.R. Brown, J. Liu, Chem. Soc. Rev. 41 (2012) 2308–2322.
[29] J. Mollmer, M. Lange, A. Moller, C. Patzschke, K. Stein, D. Lassig, J. Lincke, R. Glaser, H. Krautscheid, R. Staudt, J. Mater. Chem. 22 (2012) 10274–10286.
[30] N. Lamia, M. Jorge, M.A. Granato, F.A.A. Paz, H. Chevreau, A.E. Rodrigues, Chem. Eng. Sci. 64 (2009) 3246–3259.
[31] A. Dhakshinamoorthy, M. Alvaro, H. Garcia, Appl. Catal. A 378 (2010) 19–25.
[32] F. Karadas, C.T. Yavuz, S. Zulfiqar, S. Aparicio, G.D. Stucky, M. Atilhan, Langmuir 27 (2011) 10642–10647.
[33] S.S.Y. Chui, S.M.F. Lo, J.P.H. Charmant, A.G. Orpen, I.D. Williams, Science 283 (1999) 1148–1150.
[34] T. Loiseau, C. Serre, C. Huguenard, G. Fink, F. Taulelle, M. Henry, T. Bataille, G. Ferey, Chem. Eur. J. 10 (2004) 1373–1382.
[35] A. Boutin, M.A. Springuel-Huet, A. Nossov, A. Gedeon, T. Loiseau, C. Volkringer, G. Ferey, F.X. Coudert, A.H. Fuchs, Angew. Chem. Int. Ed. 48 (2009) 8314–8317.
[36] A. Centrone, E.E. Santiso, T.A. Hatton, Small 7 (2011) 2356–2364.
[37] A. Dhakshinamoorthy, M. Alvaro, H. Garcia, Acs Catal. 1 (2011) 836–840.
[38] P. Horcajada, S. Surble, C. Serre, D.Y. Hong, Y.K. Seo, J.S. Chang, J.M. Greneche, I. Margiolaki, G. Ferey, Chem. Commun. (2007) 2820–2822.
[39] A.K. Rappe, C.J. Casewit, K.S. Colwell, W.A. Goddard, W.M. Skiff, J. Am. Chem. Soc. 114 (1992) 10024–10035.
[40] J.J. Potoff, J.I. Siepmann, AIChE J. 47 (2001) 1676–1682.
[41] F. Dreisbach, R. Staudt, J.U. Keller, Adsorption 5 (1999) 215–227.
[42] F. Dreisbach, H.W. Losch, P. Harting, Adsorption 8 (2002) 95–109.
[43] D. Saha, Z.J. Wei, S.G. Deng, Int. J. Hydrogen Energy 33 (2008) 7479–7488.
[44] H. Furukawa, M.A. Miller, O.M. Yaghi, J. Mater. Chem. 17 (2007) 3197–3204.
[45] S. Bourrelly, P.L. Llewellyn, C. Serre, F. Millange, T. Loiseau, G. Ferey, J. Am. Chem. Soc. 127 (2005) 13519–13521.
[46] N. Heymans, S. Vaesen, G. De Weireld, Microporous Mesoporous Mater. 154 (2012) 93–99.
[47] A. Boutin, F.X. Coudert, M.A. Springuel-Huet, A.V. Neimark, G. Ferey, A.H. Fuchs, J. Phys. Chem. C 114 (2010) 22237–22244.
[48] B. Assfour, G. Seifert, Int. J. Hydrogen Energy 34 (2009) 8135–8143.
[49] T. Duren, F. Millange, G. Ferey, K.S. Walton, R.Q. Snurr, J. Phys. Chem. C 111 (2007) 15350–15356.
[50] Q.Y. Yang, C.L. Zhong, J.F. Chen, J. Phys. Chem. C 112 (2008) 1562–1569.
[51] P. He, H. Liu, Y.F. Li, Z.G. Lei, S.P. Huang, P. Wang, H.P. Tian, Mol. Simul. 38 (2012) 72–83.
[52] D.F. Sava, T.J. Garino, T.M. Nenoff, Ind. Eng. Chem. Res. 51 (2012) 612–618.
[53] G. Blanco-Brieva, J.M. Campos-Martin, S.M. Al-Zahrani, J.L.G. Fierro, Fuel 90 (2011) 190–197.
[54] A. Dhakshinamoorthy, M. Alvaro, H. Garcia, Chem. Eur. J. 17 (2011) 6256–6262.
[55] E. Haque, N.A. Khan, J.E. Lee, S.H. Jhung, Chem. Eur. J. 15 (2009) 11730–11736.
[56] S. Keskin, T.M. van Heest, D.S. Sholl, ChemSusChem 3 (2010) 879–891.
[57] O. Khvostikova, B. Assfour, G. Seifert, H. Hermann, A. Horst, H. Ehrenberg, Int. J. Hydrogen Energy 35 (2010) 11042–11051.
[58] S. Basu, M. Maes, A. Cano-Odena, L. Alaerts, D.E. De Vos, I.F.J. Vankelecom, J. Membr. Sci. 344 (2009) 190–198.
[59] K.L. Kauffman, J.T. Culp, A. Goodman, C. Matranga, J. Phys. Chem. C 115 (2011) 1857–1866.
[60] S. Bordiga, L. Regli, F. Bonino, E. Groppo, C. Lamberti, B. Xiao, P.S. Wheatley, R.E. Morris, A. Zecchina, Phys. Chem. Chem. Phys. 9 (2007) 2676–2685.
[61] A.C.C. Chang, S.S.C. Chuang, M. Gray, Y. Soong, Energy Fuels 17 (2003) 468–473.
[62] A. Lyubchyk, I.A.A.C. Esteves, F.J.A.L. Cruz, J.P.B. Mota, J. Phys. Chem. C 115 (2011) 20628–20638.
[63] N.A. Ramsahye, G. Maurin, S. Bourrelly, P.L. Llewellyn, T. Loiseau, C. Serre, G. Ferey, Chem. Commun. (2007) 3261–3263.
[64] D. Farrusseng, C. Daniel, C. Gaudillere, U. Ravon, Y. Schuurman, C. Mirodatos, D. Dubbeldam, H. Frost, R.Q. Snurr, Langmuir 25 (2009) 7383–7388.
[65] H. Frost, T. Duren, R.Q. Snurr, J. Phys. Chem. B 110 (2006) 9565–9570.